Neuron
Neurotechnique

Fast Three-Dimensional Fluorescence Imaging of Activity in Neural Populations by Objective-Coupled Planar Illumination Microscopy

Terrence F. Holekamp,[1] Diwakar Turaga,[1] and Timothy E. Holy[1,*]
[1]Department of Anatomy and Neurobiology, Washington University in St. Louis School of Medicine, 660 South Euclid, St. Louis, MO 63110, USA
*Correspondence: holy@wustl.edu
DOI 10.1016/j.neuron.2008.01.011

SUMMARY

Unraveling the functions of the diverse neural types in any local circuit ultimately requires methods to record from most or all of its cells simultaneously. One promising approach to this goal is fluorescence imaging, but existing methods using laser-scanning microscopy (LSM) are severely limited in their ability to resolve rapid phenomena, like neuronal action potentials, over wide fields. Here we present a microscope that rapidly sections a three-dimensional volume using a thin illumination sheet whose position is rigidly coupled to the objective and aligned with its focal plane. We demonstrate that this approach allows exceptionally low-noise imaging of large neuronal populations at pixel rates at least 100-fold higher than with LSM. Using this microscope, we studied the pheromone-sensing neurons of the mouse vomeronasal organ and found that responses to dilute urine are largely or exclusively restricted to cells in the apical layer, the location of V1r-family-expressing neurons.

INTRODUCTION

Intact neural circuits are formed from many distinct cell types (Nelson et al., 2006). To understand their diverse functions, fluorescence imaging (either of calcium or voltage indicators [Baker et al., 2005]) has attracted interest for the possibility of recording from most or all of the cells in a local circuit. However, imaging neural activity at cellular resolution places significant demands on the instrumentation used to collect the fluorescence signals. The three-dimensionality of intact neural tissue requires methods capable of resolving depth, a procedure often called optical sectioning. Conventionally, optical sectioning is achieved by some variant of laser-scanning microscopy (LSM), such as two-photon or confocal microscopy.

Unfortunately, a substantial disadvantage of LSM is its relatively slow acquisition over fields with many neurons, especially when compared with the timescale of neural activity. The limits on imaging speed by LSM are not technological in origin, as strategies for rapid point-scanning have been developed (Nguyen et al., 2001; Lechleiter et al., 2002; Salome et al., 2006; Gobel et al., 2007; Vucinic and Sejnowski, 2007). Instead, the fundamental limits arise from saturation of fluorescence emission: within the focal spot, illumination intensity is sufficiently high that decay from the excited state is the rate-limiting step in each fluorophore's excitation-emission cycle (Pawley, 2006) (see Supplemental Data). To collect enough photons, the laser is thus forced to dwell over each pixel for a minimum period of time (typically 0.1–10 μs, depending on fluorophore concentration and signal-to-noise requirements). This implies that reconstructing an image with $\sim 10^6$ pixels typically requires on the order of 1 s, offering inadequate temporal resolution for recording neuronal action potentials or other rapid processes. This situation sets up a tradeoff between signal-to-noise ratio, temporal resolution, and scanned field size. Such tradeoffs are mitigated when multiple pixels are sampled in parallel, a principle used in slit scanning (Masters and Thaer, 1994), spinning disk (Petran et al., 1968; Lichtman et al., 1989), and Moiré pattern structured illumination microscopes (Neil et al., 1997), but these approaches incur additional penalties in photobleaching and phototoxicity because the entire tissue volume is illuminated just to image a single plane (Murray, 1998; Conchello and Lichtman, 2005; Pawley, 2006).

Here we pursue an alternative approach to optical sectioning that avoids the tradeoffs between field size, signal-to-noise ratio, and imaging speed inherent in LSM. We then apply this technique to the study of the mouse accessory olfactory system, which presents a striking example of cellular diversity and a corresponding need to study large neuronal populations. The sensory neurons of this system reside in the mouse vomeronasal organ (VNO), in a neuroepithelium ~10 cell bodies thick in which each neuron sends a dendrite to the surface of the tissue; the signal transduction machinery is localized to the tip of the dendrite (Liman et al., 1999) and is the point at which chemical stimuli are detected (Figure S1). This detection is carried out by G protein-coupled receptors (Dulac and Torello, 2003). Each cell expresses just one or a few types of receptor proteins chosen from two large gene families, V1r and V2r, together comprising ~250 members (Dulac and Torello, 2003; Shi and Zhang, 2007). These two gene families are spatially segregated, with V1r-expressing cells residing near the surface of the sensory epithelium, while V2r neurons occupy the basal region. This segregation is maintained in the first synaptic junction in the accessory olfactory bulb (AOB), with V1r cells projecting exclusively to the

rostral AOB and V2r terminations confined to the caudal zone (Mombaerts, 2004). While this genetic and anatomic separation has been well studied, it remains unknown whether these two receptor families play different roles in behavioral responses or if there are categorical distinctions between them in terms of chemical sensitivity. Our imaging data revealed a receptor-family-level specialization in stimulus selectivity among these neurons.

RESULTS

Objective-Coupled Planar Illumination Microscopy

Conventionally, illumination in a fluorescence microscope is delivered through the same lens used for imaging; optical sectioning is achieved using pinholes or nonlinear optics. We instead achieved optical sectioning by illuminating the focal plane with a sheet of light delivered orthogonally to the detection axis (Figures 1A and 1B). The illumination sheet was generated by collimating the output of a single-mode optical fiber and then passing it through a cylindrical lens, creating a gradual waist whose line focus was positioned in the center of the field of view and in the focal plane of the objective. This arrangement allows the entire focal plane to be imaged at once, circumventing the tradeoffs faced by LSM between field size and speed.

Intact neural circuits are inherently three dimensional, so studies of neural populations would benefit greatly from imaging strategies that can quickly acquire information about activity throughout an entire volume (Gobel et al., 2007; Vucinic and Sejnowski, 2007). To achieve fast three-dimensional imaging, we coupled the illumination optics to the objective, so that both can be translated together using a piezoelectric manipulator (Figure 1A). In contrast to related approaches (Fuchs et al., 2002; Huisken et al., 2004; Dodt et al., 2007), this allows us to rapidly scan the tissue in the depth dimension without moving the sample. We call this approach objective-coupled planar illumination (OCPI) microscopy. Three-dimensional image stacks of the labeled VNO reveal that hundreds or thousands of neurons can be imaged in a stack acquired in just 2 s (Movie S1).

To insure that neither the illumination beam nor emitted light propagates through long distances in tissue, we tilted the microscope so that both illumination and optic axes are ~45° relative to a horizontally mounted sample (Figures 1B and 1C). By this means, the superficial layers of the sample are accessible to both illumination and imaging.

Optical Sectioning by Planar Illumination

The thickness of this sheet of excitation light can be constrained to a few microns throughout the optical field (see Supplemental Data), so that effective optical sectioning is achieved in thick samples (Figures 1D and 1E). To quantify the degree of optical sectioning, we imaged fluorescent beads in agarose. The three-dimensional image of a 2 μm bead was quite compact (Figure S1A), with maximum extension occurring along the objective's axial dimension due to the thickness of the light sheet. The axial thickness depends on the lateral displacement from the waist of the planar sheet (which in this case forms a line, see Supplemental Data) but varied only between 3.5 and 5 μm even over field sizes as large as hundreds of microns (Figure S1B). We note that this axial resolution is comparable or superior to that of confocal microscopy (~5 μm) using a wide-field objective of this numerical aperture (NA 0.5). When imaging in tissue, increasing depth leads to image degradation due to aberrations and scattering. Because fluorophores are excited by a single-photon process, scattering poses a more significant limitation on resolution with increasing depth for planar illumination than for two-photon microscopy.

Detection of Fast Neuronal Events over Wide Fields

To evaluate the benefits of planar illumination for fast imaging, we tested whether fast neural events could be detected over a wide field. Mouse vomeronasal sensory neurons (VSNs) were labeled with the calcium-sensitive fluorescent dye Oregon green BAPTA-1 (Experimental Procedures and Figure S2). A field ~700 μm × 100 μm, containing at least 88 cells was imaged at 200 frames/s with a signal-to-noise ratio adequate to detect very small (~0.2%) changes in fluorescence (Figure 2A). Small, rapid increases in fluorescence were seen in many cells (Figure 2B), likely reflecting the spontaneous activity of these neurons (Holy et al., 2000). Examination of these traces at higher temporal resolution (Figures 2C and 2D) revealed that these intensity changes consisted of a sequence of abrupt increases followed by a more gradual decay. Analysis of these transients by temporal deconvolution (see Supplemental Data) recovered individual events (Figures 2C–2E) that occur at rates as high as ~20 Hz. This is comparable to the typical maximum firing rates and interspike intervals observed in VSNs by extracellular electrode recording (Figures 2F and 2G). Therefore, from their magnitude (~1%; Yaksi and Friedrich, 2006), abrupt onset, and inter-event timing, it seems likely that these events reflect individual action potentials.

Previous studies using LSMs to reconstruct action potentials from calcium transients have been unable to resolve individual action potentials above firing rates of 1–4 Hz and/or have been restricted to fields of view on the scale of a single neuronal cell body (Kerr et al., 2005; Yaksi and Friedrich, 2006). In contrast, we resolve putative action potentials at firing rates of tens of Hertz over a field with nearly 100 neurons, with signal-to-noise ratios between 10- and 100-fold better than have been reported with fast two-photon microscopy (Cossart et al., 2003; Yaksi and Friedrich, 2006; Gobel et al., 2007). During long bursts, calcium dyes could become saturated and yield progressively smaller fluorescence changes (Yaksi and Friedrich, 2006). The issue of systematic action potential detection under these circumstances deserves further study.

Photobleaching

For long-term, three-dimensional imaging, a major advantage of OCPI is its far lesser rate of photobleaching when compared with confocal microscopy (Figure 3). Hundreds of three-dimensional image stacks can be acquired with only minimal photobleaching (Figures 3A–3C). A quantitative comparison between OCPI and confocal microscopy, using fluorescein beads and matching the number of collected photons per bead, revealed an ~100-fold difference in bleaching rate (Figure 3D). OCPI's advantage arises because illumination is restricted to the focal plane and does not bleach out-of-focus dye.

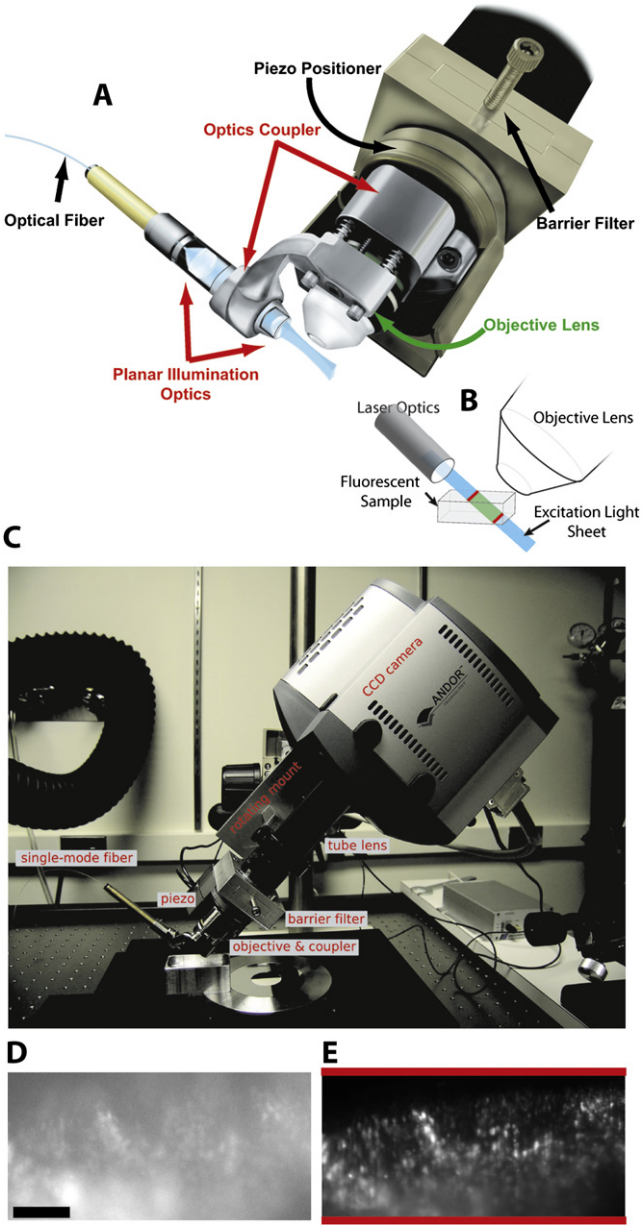

Figure 1. Objective-Coupled Planar Illumination Microscopy

(A) OCPI microscope schematic. Excitation light from a laser arrives via optical fiber and is shaped by two lenses into a thin sheet of light (~3–5 μm thick in the objective field). Sectioning is accomplished by aligning this light sheet with the objective focal plane, preventing fluorescence excitation in out-of-focus regions. Illumination optics are coupled to the objective lens, maintaining alignment with the objective focal plane during z-axis scanning with a piezoelectric positioner. Objective lens and illumination optics are designed for water immersion. Boom arm and rotating mounting adaptor allow the orientation of the microscope to be adapted to the needs of the preparation.

(B) Schematic showing the orientation of tissue, objective, and illumination optics.

(C) Labeled photograph of the complete OCPI microscope.

(D) A single image frame of fluorescently-labeled mouse vomeronasal sensory epithelium (see text and Experimental Procedures for animal preparation) using conventional wide-field fluorescence illumination shows significant out-of-focus fluorescence signal, which obscures visualization of individual neurons.

(E) The same optical field shown in (D) using objective-coupled planar illumination reveals individual neurons and demonstrates the optical sectioning capabilities of OCPI.

Scale bars, 100 μm.

Sensory Responses of Vomeronasal Neurons by OCPI Microscopy

Three-dimensional imaging was used to record from a large population of VNO neurons to probe their responses to chemical stimulation. Calcium dye-labeled vomeronasal neuroepithelia from male mice were excised and mounted with the sensory surface directly exposed to continuously flowing Ringer's solution. Chemical stimuli, including diluted urine, high-concentration potassium, and Ringer's solution control, were substituted for superfusion during multiple trials that were interleaved and presented in random order (Figure S3). Stacks of 40–50 frames (5 μm separation between frames) were acquired over 2 s, with a new stack commencing every 6 s. On the basis of VNO cell volume, each image stack contained data from well over 1000 simultaneously recorded neurons (see Experimental Procedures); however, partly because of the dense packing and ubiquity of labeling, not all of these neurons had clearly visible cell boundaries. While temporal information from spontaneous activity or sensory responses (Movie S2) could in principle be used to distinguish a cell from its neighbors, we conservatively defined regions of interest (ROIs) only for spatially distinct neurons (Figures 4A and 4B; also see Experimental Procedures). In each of six preparations, we defined between 200 and 700 ROIs, with a total of 2125 across all six experiments.

Presentation of elevated potassium or dilute urine stimuli triggered reproducible increases in fluorescence in many VSNs (Figures 4C–4I). To quantify stimulated activity, we first calculated normalized stimulated intensity changes ($\Delta F/F$) for each stimulus presentation in ROIs corresponding to individual neurons (Figures 4D and 4E). Using a t test to compare peak $\Delta F/F$ between urine stimuli and control Ringer's solution across stimulus repeats, we found that 817/2125 (38%) responded (see Experimental Procedures) to 100-fold diluted female mouse urine and 582 (27%) responded to male mouse urine. Of these neurons, 1433 were also tested at 1:1000 and 1:10,000 urine concentrations. At these concentrations, urine stimuli activated only a small subset of the neurons (female, 1:1000, 47 [3.3%]; male, 1:1000, 20 [1.4%]; female, 1:10,000, 39 [2.7%]; male, 1:10,000, 12 [0.8%]). Some were highly selective for urine from one sex over the other (Figure 4D; 38 neurons responded to 1:1000 female mouse without responding to 1:100 male mouse urine, and 15 displayed the converse selectivity), similar to previous findings using multielectrode arrays (Holy et al., 2000). Very high sensitivity and selectivity tended to be the exception rather than the norm, with only a few percent of neurons displaying clear responses to either sex at 1000-fold dilutions (Figure S4).

Regional Responsivity in the VNO

Inspection of image (Figures 5A–5D) data suggested that neurons throughout the VNO showed fluorescence increases to high potassium but that urine-responsive neurons tended strongly (and perhaps exclusively) to be located in apical regions of the tissue. To test this systematically, we examined how the

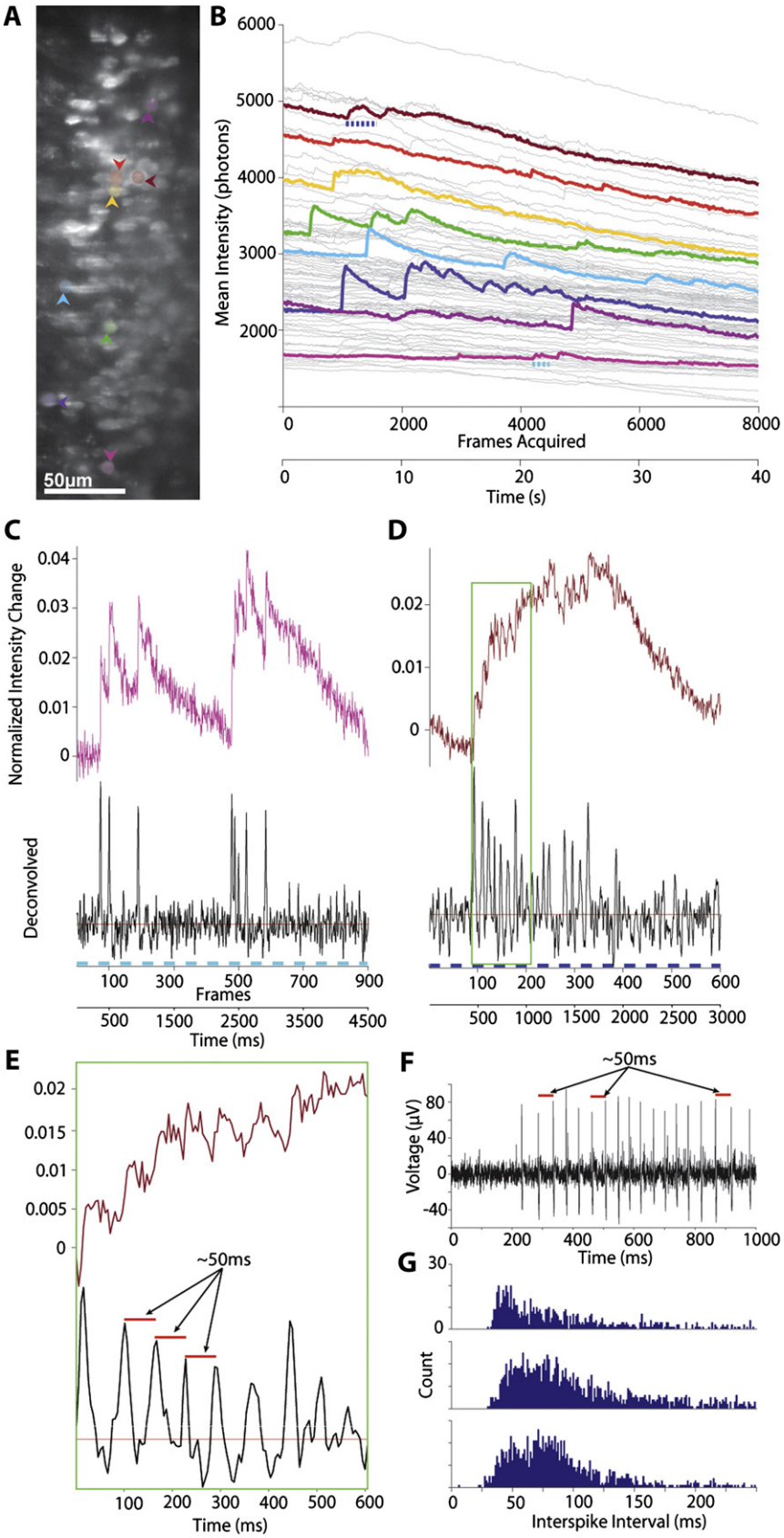

Figure 2. High-Speed Calcium Imaging of Many VNO Neurons Simultaneously in a Single Optical Plane

(A) Section of a single frame from a 40 s movie of VNO sensory neuron cell bodies imaged over a 1004 × 140 pixel field at 200 Hz. Cellular fluorescence intensities were analyzed in regions of interest (ROIs), with a few illustrative cells marked with color highlighting and arrows. Scale bar, 50 μm.

(B) Time courses of the fluorescence intensity for 88 cells in the area imaged in (A). Intensity traces from the subset of cells marked in (A) are coded by color. The transients reflect neuronal activity; note that two adjacent neurons in (A) show different transients in (B). The gradual decline in fluorescence intensity is due to photobleaching; on the order of 10^9 photons were collected from each cell during the acquisition period.

(C–E) A detailed examination of calcium transients in two selected periods, marked by blue dashed lines in (B), illustrates the extraction of fast neuronal firing from whole-field images. Raw normalized calcium fluorescence ([C and D], top) is temporally deconvolved ([C and D], bottom) to infer the timing of individual putative action potentials. (E) shows higher-resolution detail from a firing burst from (D); several transients separated by ~50 ms are marked.

(F) A typical extracellular electrical recording from a VNO neuron during burst firing.

(G) Interspike interval histograms from three individual cells recorded with extracellular electrodes; many cells fire bursts (Holy et al., 2000), with a typical interspike interval of ~50 ms.

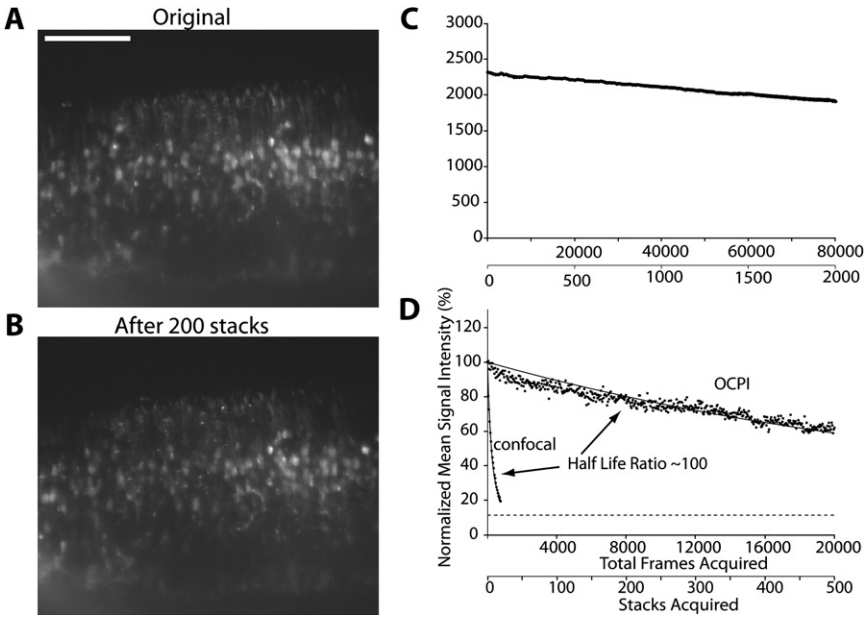

Figure 3. Reduced Photobleaching by Selective Illumination of the Focal Plane

(A and B) Images from live excised VNO sensory epithelium loaded with Oregon green BAPTA-1. (A) Initial image from a calcium imaging experiment during which 40-frame stacks were taken every 6 s. (B) shows the same optical section presented in (A) after acquisition of 200 stacks/ 8000 frames. Grayscale contrast limits are the same in (A) and (B).

(C) Plot of mean signal intensity over time for the uppermost z-plane of each stack from an 80,000-frame (~4.5 hr) experiment. Regression slope indicates the average photobleaching rate is ~0.0002% intensity lost per frame acquired.

(D) Controlled comparison of photobleaching rates reveals much slower bleaching by planar illumination than with a confocal microscope (Olympus FV1000). Repeated stacks (40 1M-pixel frames) were acquired of agarose-embedded FITC-dyed beads (2 μm diameter) with a 20× 0.5 NA objective. Laser intensities and scanning conditions were set to acquire ~4000 photons in the brightest pixels of the initial image. Shown are mean signal intensities; decay rates were estimated using an exponential model with an unbleachable component indicated by the dashed line (see Experimental Procedures).

Scale bar, 100 μm.

neuronal response (*ΔF/F*) to high potassium, Ringer's, and female and male mouse urine depended on the depth of the cell. Peak *ΔF/F* was averaged over six trials to obtain a single number characterizing each neuron and stimulus pair. For two preparations in which the tissue surface could be unambiguously identified, high potassium triggered substantial responses in ROIs over the entire range of depths, and Ringer's solution failed to induce substantial responses. Dilute urine stimuli also led to fluorescence increases, but only for ROIs in roughly the upper 50–60 μm of tissue, with the strongest responses to urine confined to the top 30 μm (Figures 5E and 5F). Thus, when evaluated in terms of single neurons, responses to diluted urine were restricted to the apical layers.

To eliminate possible confounds due to ROI placement (which were apically biased due to superior optical resolution at shallow depths), we also measured the fluorescence changes as a function of depth, averaging laterally across voxels of the same depth in tissue (see Figure S5 and Experimental Procedures). This gave equal weight to all voxels, independent of the ability of a human observer to segregate them into single neurons. As with the ROI-based analysis, this showed that, while high potassium activates cells at all depths, urine from either sex failed to substantially stimulate the basal regions (Figures 5G and 5H).

These results are consistent with the interpretation that most or all of the activity in response to urine stimuli was confined to apical cells, which express V1rs. They are also consistent with results we had obtained earlier using a different technique, wide-field imaging of the AOB, described below.

In Vivo Imaging of Sensory Nerve Terminals

The boundary between V1r- and V2r-expressing regions in the VNO is somewhat irregular, but their axon terminals target distinct regions of the AOB (Dulac and Torello, 2003). To take advantage of this clear separation, we developed a preparation inspired by previous calcium-imaging studies in the main olfactory system (Friedrich and Korsching, 1997; Wachowiak and Cohen, 2001). We inserted a thin polyimide tube into the VNO of an anesthetized, tracheotomized mouse (see Experimental Procedures) and continuously flowed Ringer's or chemical stimuli through this tube. The AOB was exposed through a craniotomy and removal of the overlying cortex, and a fluorescence macroscope (Ratzlaff and Grinvald, 1991) was used to record calcium transients associated with synaptic release from the terminals of the sensory neurons in the AOB. We thereby recorded activity in the AOB triggered by chemical stimulation of the VNO. While macroscope imaging lacks the depth resolution of OCPI microscopy, it was able to readily distinguish the rostral/caudal divisions of the AOB.

Images of the AOB were processed by masking nonfluorescent regions and smoothing and then were used to generate colorized mean *ΔF/F* images (Figure 6, top) like those calculated for VNO data. As expected, potassium produced activation throughout both zones of the AOB. In agreement with results in the VNO, urine strongly activated only the rostral zone, with no discernable increase in fluorescence in the caudal zone. Periods during presentation of negative control Ringer's solution showed a diffuse mild depression, most likely an artifact of photobleaching, which occurred at a comparable rate (e.g., note similar decline in potassium and urine responses; Figure 6, bottom). ROIs placed in each zone of the AOB revealed reproducible responses to urine in the rostral but not caudal zone (Figure S6).

Thus, imaging neural responses at the AOB, where V1r and V2r axon terminals are distinct, also supports the conclusion that

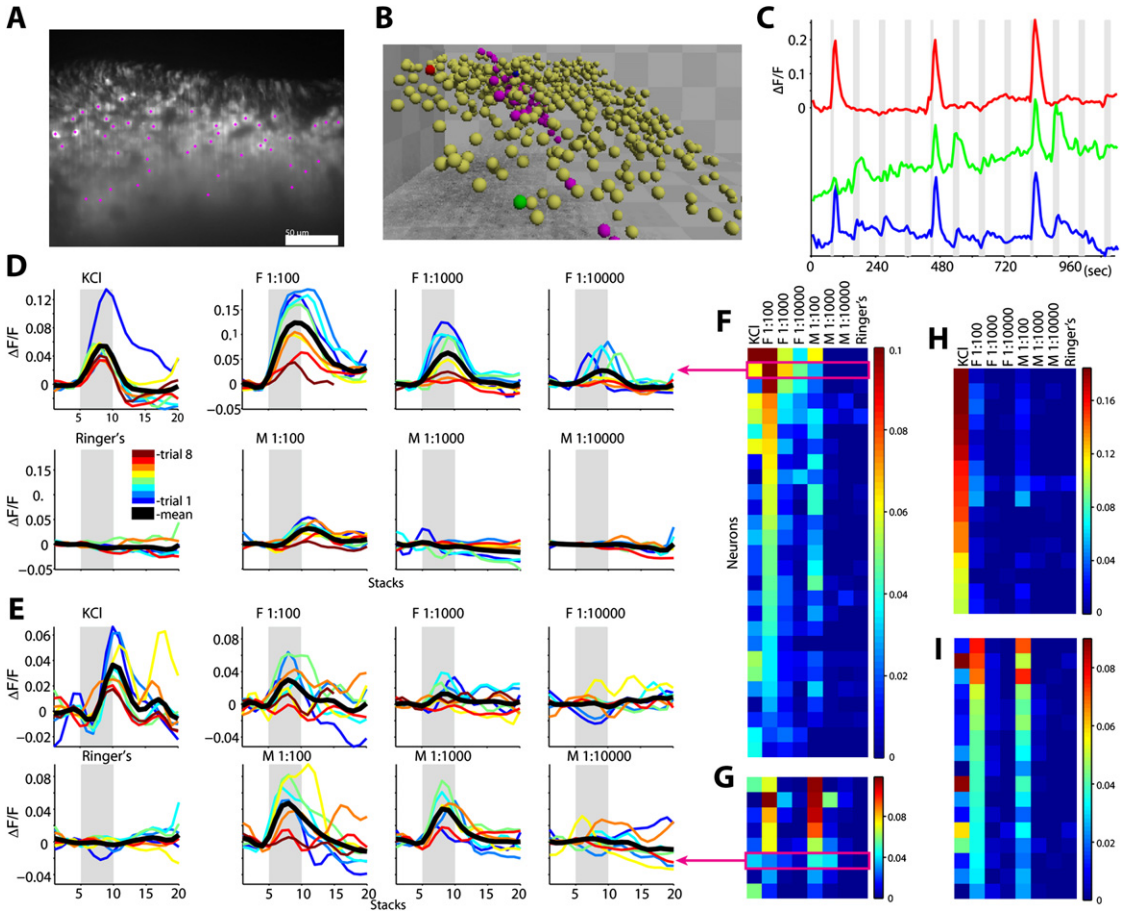

Figure 4. Probing Responses to Chemical Stimuli of Single VNO Neurons by High-Speed Three-Dimensional Calcium Imaging

(A) Intact VN epithelium labeled with Oregon green BAPTA-1; single optical section by planar illumination. Purple dots indicate position of regions of interest (ROIs) corresponding to single neurons.

(B) Three-dimensional rendering of the ROI positions for the entire 40-image stack. ROIs drawn in purple were in the single section pictured in (A). Each checker is 100 μm on a side. Sensory surface of the tissue is at the top.

(C) Normalized fluorescence change versus time for three ROIs indicated in red, green, and blue in panel (B). Vertical gray bars indicate periods of stimulation, a thrice-repeated cycle of high potassium (50 mM), female mouse urine diluted 1:100 in Ringer's solution, 1:100 male mouse urine, and Ringer's solution (negative control).

(D and E) Time course of fractional intensity changes induced by various stimuli for two selected neurons in a different preparation. Responses on single trials (thin lines) and the across-trial mean (thick black line) are shown. Period of stimulus delivery (valve opening) marked in gray. Over the course of an hour of continuous imaging (~600 stacks), the amplitude of the responses decreased due to phototoxicity.

(F–I) Colorized activity profile for selected cells showing sensitivity or selectivity for particular stimulus. Rows correspond to individual neurons, and columns represent different stimuli. Colorbars indicate fraction intensity change scale. (F) shows cells exhibiting high sensitivity (down to 1:10,000-fold diluted in Ringer's solution) and/or selectivity (up to 1:1000 selective over male) for female mouse urine. (G) presents cells exhibiting sensitivity (down to 1:1000 dilution) or selectivity (up to 1:10 over female) for male mouse urine. (H) presents cells showing maximum stimulated changes in fluorescence in response to 50 mM KCl. (I) shows cells with large stimulated changes in response to urine from both sexes. Stimuli for (G) and (I) are identical to those in (F) and (H).

urine pheromones activate predominantly, or perhaps exclusively, V1r-expressing neurons.

DISCUSSION

OCPI for Functional Neuronal Imaging

We demonstrate that OCPI is, in several respects, uniquely well-suited for imaging neuronal activity: it enables optical sectioning, large signal-to-noise ratios, minimal photobleaching, and fast imaging to all be achieved simultaneously. Furthermore, fast three-dimensional imaging is made possible by coupling the illumination to the objective and translating both to scan the tissue. OCPI microscopy should be readily applicable to both in vitro and in vivo preparations; the access-angle requirements (Figure 1A) will necessitate a craniotomy that is ~40% longer along one axis than would be required for LSM, but this rather modest increase should not present substantial barriers to use of OCPI in vivo.

Using OCPI microscopy, we recorded simultaneously from hundreds of individual neurons for 3–4 hr periods. While such large numbers of neurons have occasionally been imaged in a single preparation (Stosiek et al., 2003; Cossart et al., 2003;

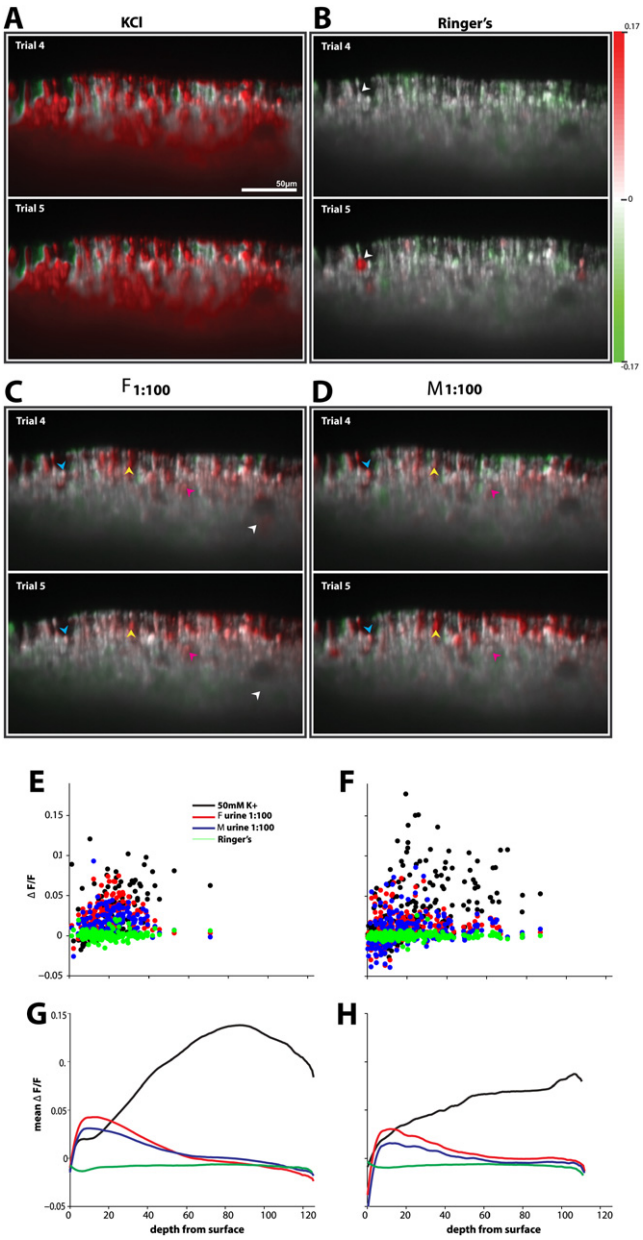

Figure 5. Imaging Reveals Patterned Responses to Pheromones in VNO

Images are color coded to represent the normalized fluorescence intensity change ($\Delta F/F$) upon stimulation (colorbar, right). Shown are two sequential trials of (A) 50 mM KCl, (B) Ringer's solution, (C) 1:100 female mouse urine, and (D) 1:100 male mouse urine. White arrow marks cell exhibiting spontaneous activity not reproducible across trials; yellow arrows mark cells that appear relatively unselective for sex; blue and pink arrows mark cells with some preference for male or female mouse urine, respectively. Colorbar indicates magnitudes of fractional intensity changes. Scale bars, 50 μm.

(E and F) $\Delta F/F$ versus depth for individual ROIs. Each neuron/stimulus combination marked with a single point; stimulus coded by the indicated color. (E) and (F) show the result for two different preparations. $\Delta F/F$ values represent averages over six trials.

(G and H) $\Delta F/F$ averaged over all voxels of a given depth. Traces are averages of ten trials.

Ohki et al., 2005, 2006; Gobel et al., 2007), previous studies have been either constrained by the signal-to-noise ratio to studying only very large (nonphysiological) fluorescence changes or have achieved this by sequential recordings from groups of tens of neurons. While sequential recording from small groups may be feasible for some studies, many investigations (e.g., studies of local circuit processing, plasticity, and systems with sparse coding) will require lengthy recordings of an entire population. Indeed, our study of the olfactory system provides such an example, because characterizing this diverse but slowly responding population of sensory neurons requires extensive recording time. The approach used here permits fluorescence changes on the scale of 1%–5% to be measured in hundreds or thousands of neurons simultaneously, over hours of recording.

High-Speed Imaging

For the data of Figure 2, each frame was collected in just 5 ms, while in Figure 4 each stack required 2 s. Despite the large difference in these timescales, both represent examples of extremely high-speed imaging. This can be seen most clearly in terms of the pixel rate: in Figure 2, we collected over a region 1004 × 140 pixels, for a total pixel rate of 28 Mpixels/s; in Figure 4, we collected over a volume 1004 × 1002 × 40 voxels, for a total pixel rate of 20 Mpixels/s. In contrast, studies of neural populations employing two-photon microscopy, even some touted as "high speed," have consistently reported voxel dwell times around 5–10 μs (Ohki et al., 2005; Yaksi and Friedrich, 2006; Gobel et al., 2007; Vucinic and Sejnowski, 2007), corresponding to a pixel rate of 0.1–0.2 Mpixels/s, at least 100-fold slower than we obtain by OCPI. There is, of course, reason to think that LSM may become faster: recent experimental results (Donnert et al., 2007) and our own theoretical estimates (Supplemental Data) suggest that two-photon microscopy may ultimately be capable of dwell times close to 1 μs while still maintaining adequate signal-to-noise ratios for neural imaging. However, even this is still at least 20-fold slower than what we report here. For two-photon microscopy, further speed enhancements are possible through multifocal excitation (Bewersdorf et al., 1998), but the gains will be limited by laser power and tissue damage: to increase speed effectively, each focal spot requires the same power (10–100 mW) typically used for a single spot, and so the excitation will cause thermal damage if multiplexed more than a few times.

These possible improvements in LSM are relatively modest by comparison to what can be expected with OCPI, in which entire frames (1 Mpixel or larger) could be taken with exposure times as short as 1 μs (see Supplemental Data). Even slower frame rates of 10–100 kHz would permit three-dimensional imaging of even the fastest biological processes (e.g., action potential propagation, the entirety of excitatory synaptic input to a single neuron) for the first time. Given recent rapid improvements in cameras and computers, it seems certain that the speed advantages of OCPI will only widen over time.

Photobleaching

By sampling from large numbers of pixels simultaneously, OCPI circumvents the tradeoff between signal-to-noise ratios and pixel rates. However, like all other imaging modalities, OCPI is still bound by the need to collect adequate photons, and thus

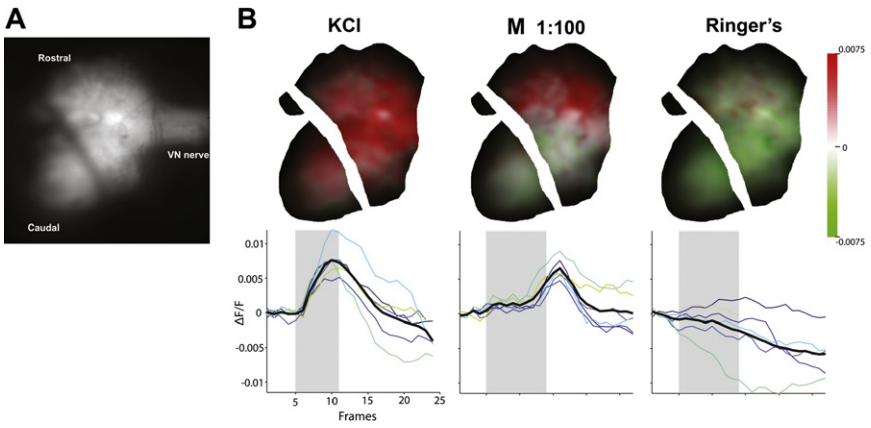

Figure 6. Pheromones Stimulate Patterned Activity in the AOB

Wide-field optical recordings of pheromone-stimulated fluorescence changes were acquired from labeled female mouse AOB in vivo.

(A) Raw fluorescence image of the AOB; the vomeronasal nerve (VN nerve) is visible.

(B) Activity upon chemical stimulation. Regions outside the AOB, as well as blood vessels, were masked. Top panels show colorized mean (six trials) $\Delta F/F$ images for control and pheromone stimuli; bottom shows corresponding temporal component to the colorized images (see Experimental Procedures). Shown are the responses to high potassium (left), dilute male mouse urine (middle), and Ringer's control (right). Individual trials are color coded, showing earlier trials as cooler colors and later trials as warmer colors. Across-trial means are shown in thick black. Stimulus period shown with gray background.

incur photobleaching, to achieve the required signal-to-noise ratio. Since the number of required photons rises as the square of the signal-to-noise ratio, high-sensitivity imaging (e.g., $\Delta F/F$ of ~0.2% as in Figures 2C and 2D) inevitably requires large numbers of photons, and hence photobleaching, no matter what imaging method is used. The appropriate balance between noise, number of acquired frames, and bleaching is largely dependent upon the individual circumstance; one perspective on OCPI is that it simply permits an unprecedented flexibility in allowing the investigator to choose how to allocate those photons over time. By comparison with other single-photon techniques, planar illumination uses photons extremely efficiently (Figure 3D) because the excitation is restricted to the in-focus plane.

Penetration Depth

One drawback of planar illumination arises from the refraction and scattering of light by tissue, progressively more prominent with increasing distance from the tissue surface. In confocal microscopy, the consequence is a limit on useful scanning depth, but shallow frames appear to be free of these effects. In contrast, every frame acquired with planar illumination captures information from both shallow and deep regions, with degraded resolution in the voxels farther from the surface. We achieve cellular resolution at least as deep as 150 μm (e.g., Figure 3A), similar to other single-photon techniques.

The depth penetration of OCPI might be significantly enhanced by improvements in both optics and fluorophores. The aberrations due to refraction at the angled tissue surface appear to be correctable by approaches that include adaptive optics (T.E.H. and D.T., unpublished data). Furthermore, since the distortion and scattering of light by tissue is reduced at longer wavelengths (Arnoldussen et al., 2000; Kim and Keller, 2003), functional imaging could benefit greatly by development of near-infrared calcium-sensitive dyes. Even without such advances, planar illumination will permit high-speed, cellular-resolution imaging of neural activity for in vitro preparations such as the retina or hippocampal slices, for the apical dendrites of cortical neurons in vivo, and for many in vivo invertebrate preparations.

Pheromone Detection by V1rs and V2rs

As a first application of this microscope, we find that, in the mouse VNO, responses to the pheromones in dilute urine are predominantly, and perhaps exclusively, generated by the apical V1r-expressing neurons. This result cannot be explained by a lack of stimulus access by the basal neurons, because the detection of pheromonal stimuli occurs at the tissue surface, in the dendritic knob containing the signal transduction machinery that each neuron sends to the apical surface (Liman et al., 1999). However, because scattering reduces resolution in the basal regions of the VNO, and weak signals in the AOB require extensive spatial averaging, we cannot entirely rule out the possibility of some responses by V2r neurons. However, because we often observe spontaneous activity in basal neurons (e.g., Figure 2 and Movie S2), it would appear that such putative responses would have to be rather rare. V2r neurons have been reported to respond to peptides secreted from glands in facial regions (Kimoto et al., 2005) and also to peptides that bind to MHC receptors (Leinders-Zufall et al., 2004), but the presence of such peptides in urine at sufficient concentration to stimulate VSNs has not been demonstrated. Similarly, some studies have suggested (Krieger et al., 1999) or found (Chamero et al., 2007) that V2rs respond to major urinary proteins (MUPs). However, a recent electrophysiological study found no evidence for VSN spiking induced by recombinant MUP1 (Kimoto et al., 2007), and another study measuring immediate-early gene expression found that the high molecular weight fraction of urine (previously found to contain MUPs) activated no more neurons in the caudal AOB than did water controls (Peele et al., 2003).

The V1r and V2r receptor families are molecularly distinct, belonging to class A and C G protein-coupled receptors, respectively (Dulac and Axel, 1995; Herrada and Dulac, 1997; Ryba and Tirindelli, 1997; Matsunami and Buck, 1997). These molecular distinctions are accompanied by well-known anatomical separations, the apical/basal zones of the VNO and the rostral/caudal zones of their projections in the AOB (Mombaerts, 2004). Dendritic processes of AOB mitral cells are largely restricted to just one of the two zones (Jia and Halpern, 1997;

Del Punta et al., 2002; Wagner et al., 2006), indicating a pervasive anatomical division at the level of the AOB. Beyond the AOB, evidence for anatomical separation is mixed, with no evidence for coarse-scale separation in mice (von Campenhausen and Mori, 2000) but with both common and segregated targets seen in opossum and rat (Martinez-Marcos and Halpern, 1999a, 1999b; Mohedano-Moriano et al., 2007). When combined with previous studies, our results also suggest a partitioning of sensory function: V2r ligands (peptides; Leinders-Zufall et al., 2004; Kimoto et al., 2005; Chamero et al., 2007) are intimately related to their source's genetic identity, while V1rs must also be capable of encoding nongenetic (e.g., social dominance) characteristics (Holy et al., 2000). Such insights highlight the importance of developing a more comprehensive understanding of the ligands for these two receptor families and for identifying specializations in the downstream neural circuitry used to process these two independent sources of sensory information about pheromones.

Summary

OCPI microscopy permits fast imaging at high signal-to-noise ratios, making it well-suited for detection and quantification of neuronal activity in intact, three-dimensional tissues. Its minimal photobleaching permits optical recordings to be made over long times. We illustrated the potential of this technique by recording simultaneously from hundreds of sensory neurons in the mammalian olfactory system. The technological requirements for OCPI microscopy are not prohibitive: aside from the microscope itself, the only significant items of equipment are a laser (which can be a low-power continuous-wave gas or solid-state laser) and a CCD camera. For this reason, OCPI microscopy should be accessible to many laboratories. Aside from imaging neuronal function, OCPI microscopy may find uses in the broader context of three-dimensional biological imaging, where it can provide resolution in depth (optical sectioning) without the long times needed to acquire image stacks by confocal or two-photon microscopy.

EXPERIMENTAL PROCEDURES

Animals

Male and female B6D2F1 mice, 6–10 weeks old (Jackson Laboratories), were used for all physiology procedures. All animals were housed and handled in accord with practices approved by the Washington University Animal Studies Committee. Mice were kept on a 12/12 hr light/dark cycle and given ad lib access to food and water at all times.

Urine Collection

Fresh frozen urine was collected from male or female BALB/c mice by housing them in mesh-bottomed cages suspended above an open-topped insulated tub filled with liquid nitrogen. Droplets of urine fell freely through the mesh cage bottoms and froze immediately upon contact with the liquid nitrogen. Custom-machined size- and shape-based filters assisted in sorting frozen urine balls from fecal pellets, crumbled food, and ice. Urine was kept frozen at −80°C until it was used for physiology experiments. At this time, urine was thawed, centrifuged to remove precipitates, and decanted before dilution to experimental concentration in Ringer's solution.

Dye Labeling

B6D2F1 mice (6–10 weeks old) were anesthetized with ketamine (87 mg/kg) and xylazine (13.4 mg/kg) and gently restrained in a supine position on a heating pad. Jaws and cheeks were retracted using custom bent-wire spring retractors, and 0.05 cc of 1% lidocaine with epinephrine (1:100,000) was injected into each cheek. The soft palette was reflected caudally, and a suction tube (0.024 inch O.D polyimide tube, Phelps-Dodge) was placed into the nasal vault opening to prevent inspiration of fluids. Dye solution was delivered to the VNO lumen through a 0.0056 inch I.D. polyimide tube (A-M Systems) passed through the nares, then carefully threaded ventrally and medially to insert through the rostral aperture of the VNO. When the tube tip was visible in the lumen, dye solution (6% 10 kDa dextran-conjugated Oregon-Green BAPTA with 0.25% Triton X; Wachowiak and Cohen, 2001) was pressure-injected into the lumen. After a 30 s delay, the tube was slowly retracted, and the procedure was repeated for the contralateral VNO. Suction and retractors were removed, and the incision was closed with tissue glue (3M Vetbond) before reviving the animal with an i.p. injection of anti-sedane (1 mg/kg). Animals were allowed to recover on the heating pad and received fluids and buprenorphine (0.05 mg/kg, s.c.) with acetominophen added to the water bottle for 1 week postoperatively. Total recovery time before physiology procedures was between 9 and 14 days.

Physiology Procedures

Excised VNO Preparation

Nine to fourteen days following the VNO dye-labeling procedure, animals were euthanized in CO_2, decapitated, and their VNOs were quickly removed and placed in ice-cold Ringer's solution (see recipe below). VNO neuroepithelium was removed from the bony capsule and separated from the tubular corpus cavernosum in fresh cold Ringer's solution and then adhered on the basal side to a nitrocellulose membrane (Millipore). Adhered tissue was mounted into a custom-machined two-part immersion chamber such that the nitrocellulose membrane was clamped between the top and bottom parts of the well with the tissue protruding into the chamber through a hole in the floor of the top segment. The tissue was continuously superfused, with stimuli alternating with Ringer's solution to achieve constant flow. All solutions were delivered at 35°C by passing through a Multichannel Systems PH01 heater tip and TC02 temperature controller. Stimulus and flush delivery timing was controlled using a ValveLink fluid handling system (Automate Scientific) with computer-controlled timing through electronically switchable pinch valves.

In Vivo AOB Preparation

In preparation for AOB imaging, animals were anesthetized with pentobarbital (50 mg/kg) and fitted with a suture-fixed endo-tracheal tube. The VNO lumen was catheterized by a short length of 0.0056 inch inner diameter polyimide tube as performed for dye labeling and fixed in position using tissue glue at the nares. This tube was connected to the ValveLink fluid delivery system (Automate) for stimulus delivery.

After stimulus tube insertion, animals were placed on a custom-built adjustable-angle stage with built-in temperature control. The scalp was reflected and the frontal and nasal bones glued to a rigid headpost. Animals were then connected to a rodent ventilator (CWE), and anesthesia was maintained by an adjustable low-flow isoflurane vaporizer (Vapomatic). The frontal and parietal bones over one cerebral hemisphere were removed, and the frontal cortex was carefully suctioned away to expose the caudal surface of the olfactory bulb. Care was taken not to disrupt the frontal or sagittal sinuses, the medial cerebral artery, or the AOB vein. Meninges overlying the AOB were usually left intact to insure adequate blood supply to the AOB. A 2% solution of low-melting-temperature agarose was poured into the cavity, and a small section of coverslip was placed over the surface of the AOB and fixed to the headpost with tissue glue. Excess agarose was suctioned away, and a suction tip was fixed to the side of the craniotomy to remove blood and CSF as it was produced during the course of the experiment. Cardiovascular status and depth of anesthesia was monitored by means of a custom-built mouse ECG amplifier connected to an oscilloscope. Stimulus delivery and Ringer's flush occurred through the polyimide tube as described for the excised VNO preparation. Stimulated AOB activity was optically recorded by a custom-built macroscope connected to a CCD camera (described below).

Solutions

Ringer's solution for physiology procedures consisted of 115 mM NaCl, 5 mM KCl, 2 mM $CaCl_2$, 2 mM $MgCl_2$, 25 mM $NaHCO_3$, 10 mM HEPES, and 10 mM glucose. High-potassium Ringer's solution for positive control stimulation

consisted of 70 mM NaCl, 50 mM KCl, 2 mM $CaCl_2$, 2 mM $MgCl_2$, 25 mM $NaHCO_3$, 10 mM HEPES, and 10 mM glucose. Solutions were bubbled at 40°C with 95% O_2, 5% CO_2 for >30 min prior to use. Final pH 7.4.

Imaging

OCPI Microscope

The OCPI microscope (Figure 1) was constructed from (top right to bottom center in Figure 1C) Andor Ixon DV885-KCS-VP Cooled EM CCD camera and PCI card, 100 mm Infinitube (Edmund Optics), custom-machined fluorescence barrier filter (Chroma HQ535/50 M) holder, peizoelectric positioner (Peizosystem Jena), Olympus 20× 0.5 NA water-immersion objective. The illumination arm (bottom center to top left in Figure 1C) consisted of a custom-machined stainless-steel adjustable illuminator/objective coupler, custom-machined laser beam-shaping optics tube that was sealed at the front aperture for water immersion with UV-curing optical adhesive (Newport), rear beam-shaping plano-convex lens (12.7 mm effective focal length, Newport), front beam-shaping circular profile cylindrical lens (8 mm effective focal length, Edmund Optics), optical fiber chuck (Newport), 488 nm-transmitting single mode unjacketed fiber, fiber coupling package (Newport), neutral density gradient wheel (Thorlabs), TTL-actuated beam shutter (Thorlabs), and a 50 mW argon gas laser (Melles-Griot).

When acquiring three-dimensional image stacks, the piezo motion was along the optic axis of the objective. Because of the tilted configuration (Figure 1), this resulted in a combined movement along both the x and z axes with respect to the tissue coordinates (see also Figure S5A). Coordinates in Figure S1 are with respect to the objective, so that x and y are lateral and z is axial.

The microscope assembly was mounted to the vertical focusing stage of a boom arm (Edmund) using a custom-machined rotating coupling adaptor built to allow angular positioning at stable, discrete values. This coupler allowed the entire microscope to be rotated with respect to the horizon and locked in position. Laser head, optics, boom arm, and microscope were mounted on an antivibration table (TMC).

Camera triggering and image acquisition was handled by custom software (which may be downloaded from http://holylab.wustl.edu). Images were stored by rapid spooling to RAM or a SATA disk RAID array. Piezo- and shutter-control voltages were supplied by a data acquisition PCI board (National Instruments); the same card acquired output signals (frame exposure, piezo position) to permit synchronization of all components.

Macroscope

In vivo calcium imaging of fluorescent mouse AOB was accomplished with a macroscope (Ratzlaff and Grinvald, 1991) constructed by coupling two camera lenses end to end with their front apertures facing each other. Coupling was achieved with a custom coupling ring that also served to hold an excitation wavelength barrier filter (Chroma # HQ535/50M). A fast short focal length lens with minimal aberration (Nikkor 35 mm F1.4) in an inverted orientation was used as the objective, while a fast, well-corrected zoom telephoto lens (Nikkor AF-S 80–200 mm F1:2.8 D) was used to project the image onto the CCD chip. An F-mount to c-mount 1.5× teleconverter (Melles-Griot) allowed a cooled CCD camera (Andor DV434-BV with 1024 × 1024 13 μm pixels) to be mounted to the rear aperture of the telephoto lens for fluorescence detection. The ratio of the focal lengths of the two lenses times the teleconversion ratio determines system magnification (3.4× to 8.6×). The lens system was mounted to a boom-arm, allowing the macroscope to look in any direction from any angle.

Since the macroscope did not have eye pieces and the field of view from the CCD is very small compared to the working distance of the lens system, it was challenging to find the correct field for imaging. To facilitate this process, a laser targeting system was developed. The CCD was swapped for a laser pen (~600 nm wavelength, with collimating optic removed), and the beam was projected through the macroscope optics. Under visual guidance, the beam was focused on the surface of the AOB, after which the laser pen was replaced by the CCD camera.

Wide-Field Illumination

Nonsectioning image of matching field (Figure 1D) was obtained by illuminating the sample from the side with a light-emitting diode (473 nm peak, Lumileds) whose output was partially collimated using a parabolic mirror (Lumileds) and delivered to the sample with a custom optical tube, diffuser, and lens assembly (Thorlabs). This light source was also used for macroscope imaging.

Analysis

VNO Single-Cell Analysis

Small, gradual changes in tissue morphology during the experiment were computationally inverted by a custom intensity-preserving nonrigid registration algorithm (to be described elsewhere). For high-speed data, small high-speed vibrational artifacts were compensated using a rigid image registration algorithm.

After registration, regions of interest (ROIs) were defined for individual cells in the first acquired stack. Mean voxel intensity within each ROI was calculated for each stack. Temporal deconvolution was performed using an optimized Weiner filter (see Supplemental Data section on temporal filtering). Average intensity within each ROI was calculated for each stack. Normalized intensity change ($\Delta F/F$) time courses were calculated for each stimulus trial, and multiple trials were averaged to qualitatively reveal the cells that repeatedly responded to a given stimulus. Single normalized response values were calculated from the maximum projections of the prestimulus and stimulated time periods for each trial. Two-tailed t tests were performed comparing these values for stimulated trials against trials of negative control Ringer's solution to determine the probability of a cell being responsive to a given stimulus. A cell was defined as responsive when $p < 0.01$ in experiments with six trials; a threshold of $p < 0.05$ was used for the single experiment with only three trials. Selectivity was defined by a cell responding to a smaller concentration of urine from one sex than the smallest concentration it responded to of the opposite sex. Selectivity ratios were calculated by dividing the smallest concentration of urine from one sex resulting in a response by the corresponding concentration of urine from the opposite sex.

A simple statistical argument can be used to estimate the likelihood that any given cell (or receptor) type in the vomeronasal epithelium was recorded. Given the probability P_r that a cell expresses a particular receptor type, and the number N of cells recorded, the probability that the given receptor type was not expressed by any of these cells is $(1 - P_r)^N$. If we take P_r simply as 1/250 (since there are ~250 functional pheromone receptor genes; this ignores the fact that different types are expressed with different abundance [Herrada and Dulac, 1997]), it may be estimated that reliable (95% confidence) recording of any particular receptor type would require a minimum of ~750 cells, similar to the maximum number of cells identified in a single experiment. If we assume a cell diameter of 10 μm and 50% packing density, our scan volume encompassed a region of ~6000 neurons in each experiment. Alternatively, for the >2000 identified single cells across experiments, this results in an estimated likelihood of $<10^{-3}$ of missing any particular receptor type. Because our ROIs are apically biased (Figures 5E and 5F), the actual likelihood is presumably even smaller for apical cells but larger for basal cells.

Voxel-Based Analysis

A voxel-based analysis was used both for generating a visual representation of the cells responding to a given stimulus (Figures 5A–5D) as well as for a systematic analysis of responsiveness versus depth (Figures 5G and 5H). Because slices were acquired in a canted orientation with respect to the tissue, we first rotated and resampled analyzed stacks to realign the stack z axis with tissue z axis. Each stimulus epoch was split into "prestimulus" and "poststimulus" periods of four stacks each (where poststimulus was timed to overlap with stimulus offset and one stack afterward). For both four-stack periods, the maximum intensity in every voxel was calculated, resulting in pre- and postmaximum projection stacks. $\Delta F/F$ stacks were then defined as (post-pre)/pre. Colorized images were created by taking the grayscale prestimulus maximum projection stack, converting it to RGB, and using each pixel's $\Delta F/F$ to reduce the blue and green (for $\Delta F/F > 0$) or red (for $\Delta F/F < 0$) color channels in proportion to the magnitude of $\Delta F/F$.

To analyze responsiveness versus depth, the tissue surface was found by an algorithm that sought the first voxel in each "column" with an intensity significantly above the offset black level. This two-dimensional rough surface was then smoothed by a median filter of 50 pixel (35 μm) diameter. Depth for each data point was then defined by its vertical position below the surface in the voxel column. Voxel-based analysis of responsiveness versus depth (Figures 5G and 5H) was performed by averaging intensities across voxels with the same depth and then calculating normalized changes upon stimulation.

In Vivo AOB Image Analysis

To assess stimulated changes in fluorescence in the AOB, first a mask was created to remove nonfluorescent regions and blood vessels (which caused

large artifacts) in the images. Two-dimensional $\Delta F/F$ images were calculated for each stimulus presentation trial in the same way described for VNO stacks. Mean $\Delta F/F$ images across six trials were then calculated. Colorized mean $\Delta F/F$ images, in which red indicates increased fluorescence and green indicates a decrease from background, were calculated to qualitatively assess the spatial extent of stimulus responses (Figure 6). Mean $\Delta F/F$ images were then used as a weighting mask to calculate the time course of fluorescence change; if $F(t)$ is a fluorescence frame at time point t and W is the weighting mask (absolute value of the average $\Delta F/F$ across trials), one temporal intensity value $V = \text{sum}(F(t).* W)/\text{sum}(W)$.

To quantitatively compare localized stimulated responses, ROIs were drawn over the rostral and caudal zones of the AOB, and normalized mean pixel intensity changes ($\Delta F/F$) were plotted across time for each stimulus (for each trial and mean across trials). ROIs were defined such that a maximum number of pixels were incorporated for spatial averaging yet positioned to eliminate any risk of sampling from the opposite zone.

Photobleaching Analysis

Bead intensities (Figure 3D) were fit to a model

$$I(n) = Be^{-rn} + U,$$

where the intensity $I(n)$ on the nth stack depends upon the bleaching rate r, the amplitude B of the bleachable component of the signal, and an unbleachable component U.

Electrical Recordings

Dissected VNO sensory epithelia were electrically recorded with an extracellular multielectrode array as described previously (Holy et al., 2000). Action potentials from individual neurons were spike-sorted using custom software.

SUPPLEMENTAL DATA

The Supplemental Data for this article (theoretical analyses, additional discussion, figures, and multimedia) can be found online at http://www.neuron.org/cgi/content/full/57/5/661/DC1/.

ACKNOWLEDGMENTS

Machining and electronics were provided partly by Charlie Hamontree and Gavin Perry of the Washington University Instrument Shop. The instrument control and acquisition software was written by Zhongsheng Guo. Rebecca Hendrickson gave advice in developing the in vivo AOB optical imaging preparation. We thank Rachel Wong, Matt Wachowiak, and Lawrence Cohen for discussions; and Paul Gray, Joseph Culver, Rachel Wong, and the anonymous referees for comments on the manuscript. Our argon laser was a gift from the Department of Anatomy and Neurobiology, Washington University School of Medicine. Funding (T.E.H.) was provided by the Edward Mallinckrodt, Jr., Foundation, the National Institutes for Deafness and Communication Disorders, the Pew Scholars Program, and the G. Harold and Leila Y. Mathers Foundation. T.E.H. conceived and designed the OCPI microscope, and D.T. performed initial prototyping. T.F.H. built and tested the OCPI microscope, developed the VNO labeling and AOB imaging preparations, and performed all of the physiological experiments. T.F.H., T.E.H., and D.T. performed the analysis. T.F.H., T.E.H., and D.T. wrote the paper. The objective-coupled planar illumination microscope is the subject of a patent filing (T.E.H. and T.F.H.).

Received: June 15, 2007
Revised: September 26, 2007
Accepted: January 7, 2008
Published: March 12, 2008

REFERENCES

Arnoldussen, M.E., Cohen, D., Bearman, G.H., and Grundfest, W.S. (2000). Consequences of scattering for spectral imaging of turbid biologic tissue. J. Biomed. Opt. *5*, 300–306.

Baker, B.J., Kosmidis, E.K., Vucinic, D., Falk, C.X., Cohen, L.B., Djurisic, M., and Zecevic, D. (2005). Imaging brain activity with voltage- and calcium-sensitive dyes. Cell. Mol. Neurobiol. *25*, 245–282.

Bewersdorf, J., Pick, R., and Hell, S.W. (1998). Multifocal multiphoton microscopy. Opt. Lett. *23*, 655–657.

Chamero, P., Marton, T.F., Logan, D.W., Flanagan, K., Cruz, J.R., Saghatelian, A., Cravatt, B.F., and Stowers, L. (2007). Identification of protein pheromones that promote aggressive behaviour. Nature *450*, 899–902.

Conchello, J.A., and Lichtman, J.W. (2005). Optical sectioning microscopy. Nat. Methods *2*, 920–931.

Cossart, R., Aronov, D., and Yuste, R. (2003). Attractor dynamics of network UP states in the neocortex. Nature *423*, 283–288.

Del Punta, K., Puche, A., Adams, N.C., Rodriguez, I., and Mombaerts, P. (2002). A divergent pattern of sensory axonal projections is rendered convergent by second-order neurons in the accessory olfactory bulb. Neuron *35*, 1057–1066.

Dodt, H.U., Leischner, U., Schierloh, A., Jahrling, N., Mauch, C.P., Deininger, K., Deussing, J.M., Eder, M., Zieglgansberger, W., and Becker, K. (2007). Ultramicroscopy: three-dimensional visualization of neuronal networks in the whole mouse brain. Nat. Methods *4*, 331–336.

Donnert, G., Eggeling, C., and Hell, S.W. (2007). Major signal increase in fluorescence microscopy through dark-state relaxation. Nat. Methods *4*, 81–86.

Dulac, C., and Axel, R. (1995). A novel family of genes encoding putative pheromone receptors in mammals. Cell *83*, 195–206.

Dulac, C., and Torello, A.T. (2003). Molecular detection of pheromone signals in mammals: from genes to behaviour. Nat. Rev. Neurosci. *4*, 551–562.

Friedrich, R.W., and Korsching, S.I. (1997). Combinatorial and chemotopic odorant coding in the zebrafish olfactory bulb visualized by optical imaging. Neuron *18*, 737–752.

Fuchs, E., Jaffe, J.S., Long, R.A., and Azam, F. (2002). Thin laser light sheet microscope for microbial oceanography. Opt. Express *10*, 145.

Gobel, W., Kampa, B.M., and Helmchen, F. (2007). Imaging cellular network dynamics in three dimensions using fast 3D laser scanning. Nat. Methods *4*, 73–79.

Herrada, G., and Dulac, C. (1997). A novel family of putative pheromone receptors in mammals with a topographically organized and sexually dimorphic distribution. Cell *90*, 763–773.

Holy, T.E., Dulac, C., and Meister, M. (2000). Responses of vomeronasal neurons to natural stimuli. Science *289*, 1569–1572.

Huisken, J., Swoger, J., Del, B.F., Wittbrodt, J., and Stelzer, E.H. (2004). Optical sectioning deep inside live embryos by selective plane illumination microscopy. Science *305*, 1007–1009.

Jia, C., and Halpern, M. (1997). Segregated populations of mitral/tufted cells in the accessory olfactory bulb. Neuroreport *8*, 1887–1890.

Kerr, J.N., Greenberg, D., and Helmchen, F. (2005). Imaging input and output of neocortical networks in vivo. Proc. Natl. Acad. Sci. USA *102*, 14063–14068.

Kim, A.D., and Keller, J.B. (2003). Light propagation in biological tissue. J. Opt. Soc. Am. A Opt. Image Sci. Vis. *20*, 92–98.

Kimoto, H., Haga, S., Sato, K., and Touhara, K. (2005). Sex-specific peptides from exocrine glands stimulate mouse vomeronasal sensory neurons. Nature *437*, 898–901.

Kimoto, H., Sato, K., Nodari, F., Haga, S., Holy, T.E., and Touhara, K. (2007). Sex- and strain-specific expression and vomeronasal activity of mouse ESP family peptides. Curr. Biol. *17*, 1879–1884.

Krieger, J., Schmitt, A., Lobel, D., Gudermann, T., Schultz, G., Breer, H., and Boekhoff, I. (1999). Selective activation of G protein subtypes in the vomeronasal organ upon stimulation with urine-derived compounds. J. Biol. Chem. *274*, 4655–4662.

Lechleiter, J.D., Lin, D.T., and Sieneart, I. (2002). Multi-photon laser scanning microscopy using an acoustic optical deflector. Biophys. J. *83*, 2292–2299.

Leinders-Zufall, T., Brennan, P., Widmayer, P., S, P.C., Maul-Pavicic, A., Jager, M., Li, X.H., Breer, H., Zufall, F., and Boehm, T. (2004). MHC class I peptides as chemosensory signals in the vomeronasal organ. Science *306*, 1033–1037.

Lichtman, J.W., Sunderland, W.J., and Wilkinson, R.S. (1989). High-resolution imaging of synaptic structure with a simple confocal microscope. New Biol. *1*, 75–82.

Liman, E.R., Corey, D.P., and Dulac, C. (1999). TRP2: a candidate transduction channel for mammalian pheromone sensory signaling. Proc. Natl. Acad. Sci. USA *96*, 5791–5796.

Martinez-Marcos, A., and Halpern, M. (1999a). Differential centrifugal afferents to the anterior and posterior accessory olfactory bulb. Neuroreport *10*, 2011–2015.

Martinez-Marcos, A., and Halpern, M. (1999b). Differential projections from the anterior and posterior divisions of the accessory olfactory bulb to the medial amygdala in the opossum, Monodelphis domestica. Eur. J. Neurosci. *11*, 3789–3799.

Masters, B.R., and Thaer, A.A. (1994). In vivo human corneal confocal microscopy of identical fields of subepithelial nerve plexus, basal epithelial, and wing cells at different times. Microsc. Res. Tech. *29*, 350–356.

Matsunami, H., and Buck, L.B. (1997). A multigene family encoding a diverse array of putative pheromone receptors in mammals. Cell *90*, 775–784.

Mohedano-Moriano, A., Pro-Sistiaga, P., Ubeda-Banon, I., Crespo, C., Insausti, R., and Martinez-Marcos, A. (2007). Segregated pathways to the vomeronasal amygdala: differential projections from the anterior and posterior divisions of the accessory olfactory bulb. Eur. J. Neurosci. *25*, 2065–2080.

Mombaerts, P. (2004). Genes and ligands for odorant, vomeronasal and taste receptors. Nat. Rev. Neurosci. *5*, 263–278.

Murray, J.M. (1998). Evaluating the performance of fluorescence microscopes. J. Microsc. *191*, 128–134.

Neil, M.A.A., Juskaitis, R., and Wilson, T. (1997). Method of obtaining optical sectioning by using structured light in a conventional microscope. Opt. Lett. *22*, 1905–1907.

Nelson, S.B., Sugino, K., and Hempel, C.M. (2006). The problem of neuronal cell types: a physiological genomics approach. Trends Neurosci. *29*, 339–345.

Nguyen, Q.T., Callamaras, N., Hsieh, C., and Parker, I. (2001). Construction of a two-photon microscope for video-rate Ca(2+) imaging. Cell Calcium *30*, 383–393.

Ohki, K., Chung, S., Ch'ng, Y.H., Kara, P., and Reid, R.C. (2005). Functional imaging with cellular resolution reveals precise micro-architecture in visual cortex. Nature *433*, 597–603.

Ohki, K., Chung, S., Kara, P., Hubener, M., Bonhoeffer, T., and Reid, R.C. (2006). Highly ordered arrangement of single neurons in orientation pinwheels. Nature *442*, 925–928.

Pawley, J.B. (2006). Fundamental limits in confocal microscopy. In Handbook of Biological Confocal Microscopy, J.B. Pawley, ed. (New York: Plenum Press), pp. 20–42.

Peele, P., Salazar, I., Mimmack, M., Keverne, E.B., and Brennan, P.A. (2003). Low molecular weight constituents of male mouse urine mediate the pregnancy block effect and convey information about the identity of the mating male. Eur. J. Neurosci. *18*, 622–628.

Petran, M., Hadravsky, M., Eggar, M.D., and Galambos, R. (1968). Tandem-scanning reflected-light microscopy. J. Opt. Soc. Am. *58*, 661–664.

Ratzlaff, E.H., and Grinvald, A. (1991). A tandem-lens epifluorescence macroscope: hundred-fold brightness advantage for wide-field imaging. J. Neurosci. Methods *36*, 127–137.

Ryba, N.J., and Tirindelli, R. (1997). A new multigene family of putative pheromone receptors. Neuron *19*, 371–379.

Salome, R., Kremer, Y., Dieudonne, S., Leger, J.F., Krichevsky, O., Wyart, C., Chatenay, D., and Bourdieu, L. (2006). Ultrafast random-access scanning in two-photon microscopy using acousto-optic deflectors. J. Neurosci. Methods *154*, 161–174.

Shi, P., and Zhang, J. (2007). Comparative genomic analysis identifies an evolutionary shift of vomeronasal receptor gene repertoires in the vertebrate transition from water to land. Genome Res. *17*, 166–174.

Stosiek, C., Garaschuk, O., Holthoff, K., and Konnerth, A. (2003). In vivo two-photon calcium imaging of neuronal networks. Proc. Natl. Acad. Sci. USA *100*, 7319–7324.

von Campenhausen, H., and Mori, K. (2000). Convergence of segregated pheromonal pathways from the accessory olfactory bulb to the cortex in the mouse. Eur. J. Neurosci. *12*, 33–46.

Vucinic, D., and Sejnowski, T.J. (2007). A compact multiphoton 3D imaging system for recording fast neuronal activity. PLoS. ONE *2*, e699.

Wachowiak, M., and Cohen, L.B. (2001). Representation of odorants by receptor neuron input to the mouse olfactory bulb. Neuron *32*, 723–735.

Wagner, S., Gresser, A.L., Torello, A.T., and Dulac, C. (2006). A multireceptor genetic approach uncovers an ordered integration of VNO sensory inputs in the accessory olfactory bulb. Neuron *50*, 697–709.

Yaksi, E., and Friedrich, R.W. (2006). Reconstruction of firing rate changes across neuronal populations by temporally deconvolved Ca2+ imaging. Nat. Methods *3*, 377–383.